

Supplementary Materials for

Interaction Driven Quantum-Hall Wedding cake-like Structures in Graphene Quantum Dots

Christopher Gutiérrez^{1,2,*,\dagger}, Daniel Walkup^{1,2,*}, Fereshte Ghahari^{1,2,*}, Cyprian Lewandowski^{3,*}, Joaquin F. Rodriguez-Nieva⁴, Kenji Watanabe⁵, Takashi Taniguchi⁵, Leonid S. Levitov³, Nikolai B. Zhitenev¹, and Joseph A. Stroscio¹

¹Center for Nanoscale Science and Technology, National Institute of Standards and Technology, Gaithersburg, MD 20899, USA

²Maryland NanoCenter, University of Maryland, College Park, MD 20742, USA

³Department of Physics, Massachusetts Institute of Technology, Cambridge, MA 02139, USA

⁴Department of Physics, Harvard University, Cambridge, MA 02138, USA

⁵National Institute for Materials Science, Tsukuba, Ibaraki 305-0044, Japan

correspondence to: joseph.stroscio@nist.gov

This PDF file includes:

- I. Methods and sample fabrication
- II. Enhanced Fermi velocity measurements
- III. Modeling the wedding cake potential
- IV. Estimating the width of the incompressible region

Figures S1 and S2

Captions for Movie S1

Other Supplementary Materials for this manuscript includes the following:

Movie S1

* These authors contributed equally to this work.

\dagger Present address: Quantum Matter Institute, University of British Columbia, Vancouver, British Columbia V6T 1Z4, Canada

I. Methods and sample fabrication

Our graphene heterostructure device consists of monolayer graphene on 20 nm thick hexagonal boron nitride (hBN) on 285 nm SiO₂/Si. Details on this device and its assembly have been reported previously (22) using a transfer method described in Ref. (32). To summarize briefly, single crystals of hBN were exfoliated onto SiO₂/Si substrates where a suitably thick flake (20 nm) was selected for further processing. Separately, monolayer graphene flakes were exfoliated onto a stack consisting of polymethyl methacrylate (PMMA)/polyvinyl alcohol (PVA)/Si. PVA is water-soluble and acts as a sacrificial layer for delaminating the graphene and allowing it to be transferred onto the target hBN/SiO₂/Si using a micromanipulator. After transferring, Cr(1 nm)/Pd(10 nm)/Au(40 nm) electrical contacts, including two sets of radial guides for STM navigation, were deposited onto the sample using standard e-beam lithography processing. The final device is annealed for several hours in 5% H₂/95% Ar at 350 °C to remove any processing residues. The sample was annealed one final time in an ultra-high vacuum chamber at 350 °C for several hours prior to STM measurements.

The graphene quantum dots (QD) were made by ionizing impurities in the hBN substrate using the STM tip, as described in Ref. (20), creating a *p*-type QD embedded in an *n*-type background (see Fig. 1A of the main text). To achieve the specific nano-patterning in our device, the global backgate voltage is first set to $V_g = 30$ V and the STM tip is retracted by 2 nm. Next, the sample voltage bias (relative to the grounded STM tip) is ramped to 5 V and held for $t = 60$ s. The strong electric field just beneath the STM tip during the 5 V pulse ionizes impurities in the hBN which redistribute themselves to cancel out the field of the global backgate. Finally, the external gate is lowered to $V_g = 5$

V (corresponding to global n -doping for our device), whence the ionized impurities in the pulsed region act as a negative local embedded gate, resulting in a local p -doped region in the graphene. For all measurements in this report, the global backgate voltage was held fixed at $V_g = 5$ V (after the QD was created).

We probe the quantum states in the graphene QD by measuring the tunneling differential conductance, $g(V_b, V_g, r, B) = dI/dV_b$, as a function of tunneling bias, V_b , back gate potential, V_g , spatial position, r , and magnetic field, B . dI/dV_b measurements were recorded via lock-in detection using an AC voltage of 2 mV at a frequency of 383 Hz with the STM feedback disengaged. All measurements were performed at $T = 4.3$ K.

Raw differential conductance curves measured on graphene quantum dots feature fine resonator state peaks superimposed on a large dispersive graphene background (20, 22) (Fig. S1, black curve). This superposition makes it difficult to image all the salient features in the data on the same color scale, for example in 2D radial maps in the main text (Fig. 2). We thus follow refs. (33, 34) and subtract a smoothly-varying background (red curve) from each dI/dV_b curve and plot the residual (blue curve), as shown in Fig. S1. The smoothly-varying background for each dI/dV_b curve is calculated by Gaussian smoothing the original data with a FWHM = 28.3 meV.

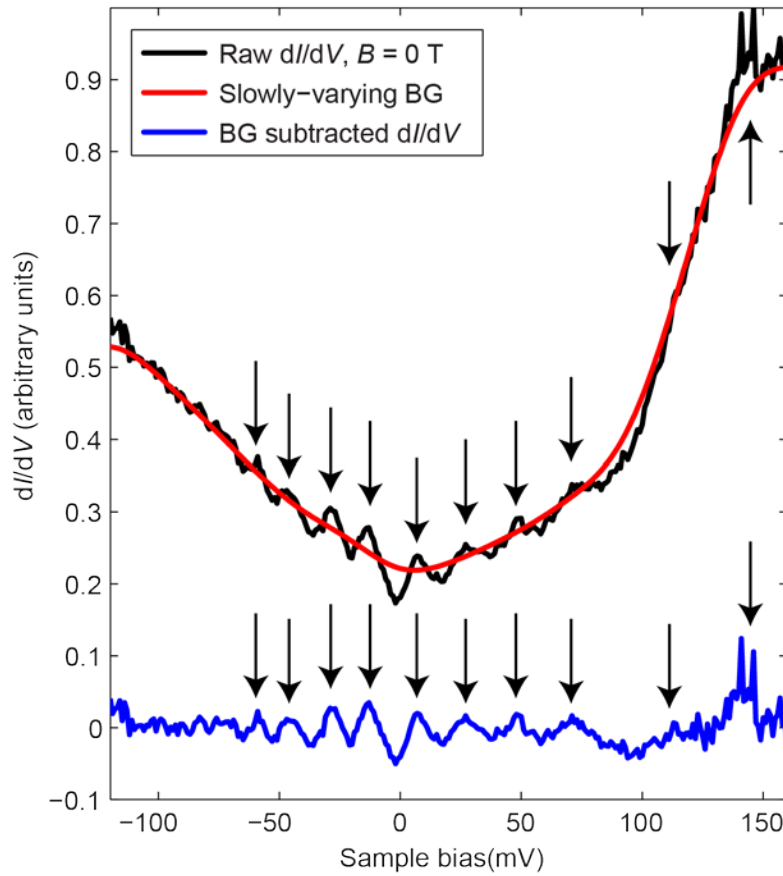


Figure S1: Original and background-subtracted differential conductance. Original dI/dV_b spectra (black line) display a slowly-varying and dispersive graphene background (BG) (red line). In order to enhance the salient features in the LDOS, such as the QD states indicated by the arrows, the BG is subtracted from the original dI/dV_b producing the blue curve, which preserves the positions of the QD resonance peaks (black arrows).

II. Enhanced Fermi velocity measurements

Close inspection of the LLs in Fig. 2J shows that the LL energy spacings are larger than expected from theory (Eq. S1) and increase with increasing magnetic field. From Eq. S1 we attribute this increase to an effective enhancement of the Fermi velocity, v_F , which we extract from our experimental spectroscopic differential conductance maps using two methods: (1) At low fields ($B < 2.5$ T), we employ Fourier transforms of the radial dI/dV maps, $\tilde{g}(q_x, q_y, V_b, V_g, B)$, to analyze quasiparticle interference (QPI) patterns in order to extract the graphene dispersion; and (2) at higher fields ($B > 1.5$ T), we use the peak positions of the characteristic graphene Landau level energies. The result of the analysis shows the Fermi velocity increasing with increased applied magnetic field.

1. QPI analysis

Surface defects and potential boundaries act as scattering sites for 2D electron gases (2DEGs) (35, 36), whereby the scattered electrons interfere with each other and appear as standing waves in the local density of states (LDOS) with a characteristic scattering wavevector, $\mathbf{q} = \mathbf{k}_f - \mathbf{k}_i$, that connects two points on a constant energy surface. The Dirac fermions within our graphene QD form quasi-bound states due to Klein scattering at the walls of the potential boundary and appear as circular standing waves (18–22). At low energies, the graphene bandstructure is composed of linear Dirac cones at the K and K' points in the first Brillouin zone (Fig. S2A). The constant energy contours (CECs) are circles of radius $k(E)$, where the momentum k depends on energy E according to the graphene dispersion $E(k) = \hbar v_F k + E_D$, where E_D is the Dirac point (Fig. S2A). The

maximum scattering wavevector, q , of the circular QPI patterns is then given by the diameter of the CEC, $q = 2k$ (Fig. S2A, right). Figure S2B displays a tomographic slice of the fast Fourier transform (FFT) of the experimental dI/dV map, \tilde{g} , recorded at $B = 0.5$ T. A linear dispersion is clearly observed, with a slope (red line, linear fit) given by $\hbar v_F/2$. Note that the Fermi energy ($V_b = 0$) cuts through the graphene valence band, confirming that the graphene QD is p -doped at its center.

2. Landau level analysis

In graphene (and other Dirac materials), the Landau level energies, ε_N , are unevenly spaced and given by the expression

$$\varepsilon_N = v_F \sqrt{2e\hbar B} [\text{sgn}(N) \sqrt{|N|}], N \in \mathbb{Z} \quad (\text{S1})$$

where N is the (integer) Landau level index, v_F is the graphene Fermi velocity, e is the elementary charge, \hbar is Planck's constant divided by 2π , B is the magnetic field, and $\text{sgn}(N)$ is the sign of the Landau level index. Figure S1C displays a dI/dV spectra recorded at the center of the GQD ($r = 0$ nm) at $B = 3$ T and displays strong peaks that correspond to the large density of states at the highly-degenerate Landau levels. The Fermi velocity is then calculated from linear fits of the LL energy, ε_N , versus the bracketed term involving the LL index in Eq. S1 (Fig. S2C, inset).

3. Discussion

Combining the measured Fermi velocities using the two methods, we find that there is an enhancement of v_F with increasing magnetic field (Fig. S2D). (The two data points at $B = 4$ T correspond to LL spectra measured inside and outside the graphene QD.) A

linear fit of the combined data yields $v_F = v_0 + \alpha B$, where $v_0 = (1.017 \pm 0.022) \times 10^6$ m/s and $\alpha = 0.124 \pm 0.011$ ms⁻¹T⁻¹ (37). We note that Fermi velocity renormalization in graphene has been observed previously at low carrier densities ($n < 10^{12}$ cm⁻²) near the Dirac point and was attributed to electronic interactions (14, 38). This is in agreement with our observations of decreasing density, for example, at $B = 4$ T (Fig. 4E main text), the density is $n = \frac{E_D^2}{\pi \hbar^2 v_F^2} \approx 0.23 \times 10^{12}$ cm⁻² (for $E_D \approx 92$ meV, $v_F \approx 1.64 \times 10^6$ m/s). This is also consistent with increased electron-electron (ee) interactions with applied magnetic fields, as evidenced by the increase in the observed Fermi velocity, the kinks in the ‘wedding cake’ spatial structure of the LLs (Fig. 2 and Fig. 4E main text), and the need for self-consistent potentials to accurately simulate the data in applied magnetic fields.

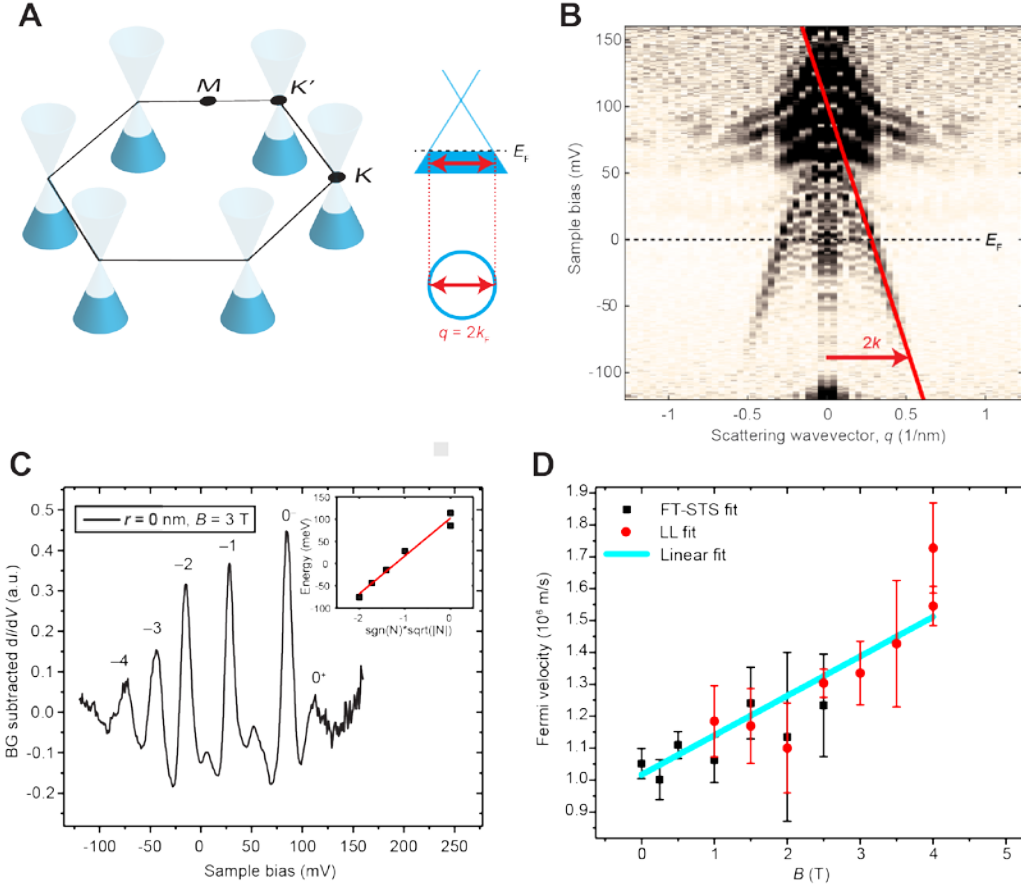


Figure S2: Magnetic field-dependence of the Fermi velocity. (A) Schematic of the low-energy band structure of graphene, displaying Dirac cones at the K/K' points. Right panel: Side-view of a single Dirac cone with the Fermi energy, E_F , crossing the valence band, signifying p -doping. The maximum scattering wavevector (red arrow) has a magnitude $q = 2k$. (B) Fourier transform scanning tunneling spectroscopy (FT-STs) map recorded at $B = 0.5$ T. A linear fit of the conical quasi-particle interference pattern (red line) yields a slope directly proportional to the graphene Fermi velocity. (C) dI/dV spectra recorded at $B = 3$ T, displaying sharp resonances at the graphene LLs. A slowly-varying, dispersive graphene background has been removed to highlight the salient features. Inset: A plot of the LL energies versus the LL index N and linear fit (red line) proportional to v_F . (D) A combined plot of the measured Fermi velocities as a function of magnetic field using the two methods displayed in (B) and (C). The Fermi velocity is seen to increase with increasing field, coinciding with the decrease in density and increasing importance of electron-electron (ee) interactions in the quantum dot system. Error bars represent one standard deviation uncertainties from linear least-squares fits to the QPI and LL plots as shown in (B) and (C), respectively.

III. Modelling the Wedding Cake potential

Here we describe the approach used to model the experimental data. Our analysis proceeds in two steps. First, an effective electrostatic potential which accounts for screening and Coulomb repulsion is calculated. Second, this potential is used as an input for the one-particle Dirac equation to produce LDOS maps shown in Fig. 4.

1. Determining the self-consistent potential and charge density

We consider graphene's Dirac electrons in the quantum Hall regime and in the presence of an external electrostatic potential $V_{\text{ext}}(r)$. We assume that the $V_{\text{ext}}(r)$ spatial variation is slow on the scale of the magnetic length l_B . The total energy of the system is a sum of contributions from the kinetic energy due to the cyclotron motion, the potential energy due to $V_{\text{ext}}(r)$, and the Coulomb energy due to electron-electron (ee) repulsion. As discussed in the main text, the wedding cake-like structure results from the competition between the kinetic energy (i.e. filling the lowest possible LL) and the potential energy due to ee repulsion and the external potential. These competing behaviors are captured by the energy functional introduced and discussed in the main text (also, see (4)):

$$E[n] = \int d^2r \left(K[n(r)] + V_{\text{ext}}(r)n(r) + \frac{1}{2} \int d^2r' V_{ee}(|\mathbf{r} - \mathbf{r}'|)n(r)n(r') \right). \quad (\text{S2})$$

Here $n(r)$ is the graphene charge density at position \mathbf{r} , and $K[n(r)]$ is the kinetic energy due to the Landau levels:

$$\frac{\delta K}{\delta n(r)} = \varepsilon_N, \quad \left(N - \frac{1}{2}\right)n_{LL} < n(r) < \left(N + \frac{1}{2}\right)n_{LL}. \quad (\text{S3})$$

Here n_{LL} is the density of a filled LL $n_{LL} = g/2\pi l_B^2$, where $g = 4$ is the LL spin-valley degeneracy. The energy of the N th LL is:

$$\varepsilon_N = \hbar\omega_c \text{sgn}(N)\sqrt{|N|}, \quad \omega_c = v_F \sqrt{\frac{2eB}{\hbar}}. \quad (\text{S4})$$

The ee interaction is given by $V_{ee}(r) = \frac{\tilde{e}^2}{r}$. Here \tilde{e} is the screened electron charge, $\tilde{e}^2 = \frac{e^2}{4\pi\epsilon_0\kappa_{ave}}$ with κ_{ave} an average dielectric constant and ϵ_0 the vacuum permittivity.

The quantum dot is defined by the potential induced by localized charges in the ionized region of the substrate $V_{\text{ext}}(r)$, offset by an electrostatic potential induced by uniform charge distribution $-n_g$ at the back gate, both of which contribute to the external potential $V_{\text{ext}}(r)$ in Eq. S2. Naturally, the total charge at the gates is much greater than the total charge in the ionized region, and the graphene-gate distance is much smaller than the size of the graphene flake. As a result, we assume that graphene screens the charge at the gate. We therefore set $n(r) = n_g + \delta n(r)$, where δn is the charge induced by $V_{\text{ext}}(r)$. The functional can then be expressed in terms of $\delta n(r)$ as:

$$E[\delta n] = \int d^2r \left(K[n_g + \delta n(r)] + \tilde{V}_{\text{ext}}(r)\delta n(r) + \frac{1}{2} \int d^2r' V_{ee}(|\mathbf{r} - \mathbf{r}'|)\delta n(r)\delta n(r') \right), \quad (\text{S5})$$

where we subtracted a constant that does not depend on δn .

For the localized charges in the ionized region, we use the potential corresponding to a point-like charge potential:

$$\tilde{V}_{\text{ext}}(r) = \frac{\tilde{V}_{\text{ext},0}}{\sqrt{1 + \frac{r^2}{r_{\text{ext}}^2}}} \quad (\text{S6})$$

with parameters $\tilde{V}_{\text{ext},0} = 1450$ meV and $r_{\text{ext}} = 85$ nm to reproduce the observed charge density and its spatial extent.

To minimize Eq. S5, we first note that the term $K[\delta n(r)]$ introduces non-linearity to the functional $E[\delta n]$. Nevertheless, $E[\delta n]$ is a concave function of $\delta n(r)$ and, as such, is amenable to gradient descent. We begin by using a trial solution $\delta n_0(r) = 0$. For each r , we compute the direction of ascending E :

$$\frac{\delta E}{\delta n(r)} = \frac{\delta K}{\delta n} [n_{\text{g}} + \delta n_k(r)] + \tilde{V}_{\text{ext}}(r) + \int d^2 r' V_{\text{ee}}(|\mathbf{r} - \mathbf{r}'|) \delta n_k(r'). \quad (\text{S7})$$

The density profile is then updated using

$$\delta n_{k+1}(r) = \delta n_k(r) - \frac{\delta E}{\delta n(r)} [\delta n_k] h, \quad (\text{S8})$$

where h is a small step size in the direction of descending energy. The procedure is continued until the minimum of the functional in Eq.(S5) is reached:

$$\frac{\delta K}{\delta n} [n_{\text{g}} + \delta n(r)] + \tilde{V}_{\text{ext}}(r) + \int d^2 r' V_{\text{ee}}(|\mathbf{r} - \mathbf{r}'|) \delta n(r') = 0. \quad (\text{S9})$$

From the solution of Eq. S7, we define the effective potential $V_B(r)$:

$$V_B(r) = V_{\text{ext}}(r) + \int d^2 r' V_{\text{ee}}(|\mathbf{r} - \mathbf{r}'|) \delta n(r'), \quad (\text{S10})$$

which is used as the input of the one-particle Dirac equation (see next section).

The charge density $n(r)$ is shown in Fig. 4B and the effective potential $V_B(r)$ for several magnetic field values is presented in Fig. 4A of the main text. In Fig. 4C we plot the effective potential $V_B(r)$ displaced by consecutive LLs energies, Eq.(S4), for $N = -14, -13, \dots, 10$. The compressible and incompressible regions corresponding to the plateaus and concave elements of the screened potential are described in the main text.

2. Solving the Dirac equation

We consider the Dirac equation for radially confined electrons in the presence of a uniform magnetic field:

$$[v \boldsymbol{\sigma} \cdot \mathbf{q} + V_B(r)] \Psi(\mathbf{r}) = \epsilon \Psi(\mathbf{r}) \quad (\text{S11})$$

Here \mathbf{q} is the kinematic momentum with components $q_{x,y} = -i\hbar\partial_{x,y} - eA_{x,y}$ and $q_z = 0$. The approach presented here follows the same reasoning as given in Ref. (24), but we reproduce and expand the discussion here for completeness.

Due to the rotational symmetry of the potential $V_B(r)$ we use the axial gauge $A_x = -By/2, A_y = Bx/2$. The eigenstates of Eq. S11 can be then expressed using the polar decomposition ansatz,

$$\Psi_m(r, \theta) = \frac{e^{im\theta}}{\sqrt{r}} \begin{pmatrix} u_1(r)e^{-\frac{i\theta}{2}} \\ iu_2(r)e^{\frac{i\theta}{2}} \end{pmatrix} \quad (\text{S12})$$

with m a half-integer number. This decomposition allows to rewrite Eq. (S11) as

$$\begin{pmatrix} V_B(r) - \epsilon & \partial_r + m/r - Br/2 \\ -\partial_r + m/r - Br/2 & V_B(r) - \epsilon \end{pmatrix} \begin{pmatrix} u_1 \\ u_2 \end{pmatrix} = 0 \quad (\text{S13})$$

Connection with an experimental measurement of conductance $g = dI/dV$ is provided via a local density of states (LDOS) $g \propto D(\epsilon, r)$. The quantity $D(\epsilon, r)$ can be conveniently written as the sum of m -state contributions $D(\epsilon, r) = \sum_m D_m(\epsilon, r)$, with

$$D_m(\epsilon, r) = \sum_{\alpha} \frac{|u_{\alpha}(r)|^2}{r} \delta(\epsilon - \epsilon_{\alpha}). \quad (\text{S14})$$

Here α labels the radial eigenstates of Eq. S13 for fixed m .

When discretizing a Dirac equation on a lattice one encounters the problem of Fermion doubling. One standard approach is to use a forward-backward difference scheme (39, 40) for approximating the partial derivatives in Eq. (S13)

$$\partial_r u_1 \approx \frac{u_1(r) - u_1(r - h)}{h}, \quad \partial_r u_2 \approx \frac{u_2(r + h) - u_2(r)}{h} \quad (\text{S15})$$

where $h = \frac{L}{N-1}$ corresponds to the discretization step size for a system of size L and N lattice sites. This requires us to specify boundary conditions on $u_1(0)$ and $u_2(L)$, which, to preserve the hermiticity of the Hamiltonian, are taken as $u_1(0) = 0$ and $u_2(L) = 0$. The latter boundary condition does not carry any consequence in context of the LDOS maps. On the other hand, the vanishing of $u_1(0)$ does matter as it forces the LDOS to vanish at the origin – an unphysical condition. As a remark, we note that this does not impact the local density of states a few step sizes away from the origin.

In order to produce spectral maps free of this artifact, while preserving hermiticity of the discretized Hamiltonian and avoiding the fermion doubling problem, we employ a simple trick: we compute the local density of states using both forward-backward and

backward-forward difference schemes and combine the two results. In the backward-forward scheme the partial derivatives from Eq. S13 take the form:

$$\partial_r u_1 \approx \frac{u_1(r+h) - u_1(r)}{h}, \quad \partial_r u_2 \approx \frac{u_2(r) - u_2(r-h)}{h} \quad (\text{S16})$$

The simulation was run on a lattice consisting of $N = 600$ sites and a system size $L = 430$ nm. Level broadening was chosen as $\gamma = 2.4$ meV. The range of angular momenta summed was estimated as to include all states that give rise to physical features in the LDOS of region of interest. As in earlier works, the contribution of spurious states present due to a finite system size were excluded.

IV. Estimating the width of the incompressible region

The width of the observed incompressible ring can be estimated from the functional in Eq. S5 following the approach of Ref. (5). In the absence of the kinetic energy term, $K[n(r)]$, the system is fully compressible and Eq. S5 predicts a smooth charge density profile that spans the entire QD (the dashed line in Fig. 4B). Once $K[n(r)]$ is restored, Eq. S5 predicts flat regions as illustrated in Fig. 4B, with the charge density profile shown as the solid line. These regions correspond to incompressible rings in $n(r)$, formed between LLs crossings with the Fermi level. The incompressible region size can be estimated by considering a dipolar strip of width l and optimizing l to minimize Coulomb repulsion between graphene electrons. Qualitatively the resulting value of l is such that the built-in electric field within the strip, $\tilde{e}Ea \sim \tilde{e}^2 \frac{dn}{dr} l^2$ matches the LL separation, $\Delta\epsilon_{LL}$. Here we provide a derivation of the Eq. 4 used in the main text, which provides a quantitative estimate of the dipolar strip width.

Following Ref. (5), we write an electric potential of a two-dimensional electron system (2DES) containing the incompressible region in terms of suitably chosen harmonic functions:

$$\phi(z) = \text{Im} \left[\frac{u_1}{\pi} \ln \left((z^2 - a^2)^{\frac{1}{2}} + z \right) + u_2(z^2 - a^2)^{1/2}z + u_3z \right], \quad y \geq 0 \quad (\text{S17})$$

where z is a complex variable $z = x + iy$ with x replacing r and y denoting the vertical coordinate perpendicular to the 2D layer. Here, following (5), we consider a quasi-1D linear geometry in which potential and density depend on one of the Cartesian coordinates in the plane but do not depend on the other coordinate. This corresponds to the limit of the incompressible ring in our QHE droplet being much narrower than the droplet radius. We assume that the incompressible region occurs at $-a < x < a$.

We note that, while the main ingredients in our problem are the same as in that analyzed in Ref. (5), there is a slight difference in the geometry that leads to extra numerical factors in the final result. Namely, Ref. (5) considers a 2DES with proximal top gates parallel to it and a dielectric beneath it, and obtains an incompressible strip of width greater than the distance to the gates. Here, in contrast, the incompressible strip width is small compared to the distance to the back-gate, and therefore we have to analyze a 2DES with dielectric beneath it and vacuum above it. This problem is equivalent to a more symmetric problem with a dielectric on both sides of the 2DES of an effective dielectric constant $\kappa_{ave} = (\kappa + 1)/2$, where κ is the permittivity beneath the 2DES. In this case, the potential of a charge plane $\sigma(x)$ representing 2DES has mirror symmetry with respect to the plane, given by Eq. S17 at $y > 0$ and by an identical function beneath the plane such that the potential is overall $y/-y$ symmetric. For clarity

in what follows we perform the calculation in terms of a screened electron charge $\tilde{e}^2 =$

$$\frac{e^2}{4\pi\epsilon_0\kappa_{ave}}.$$

The charge density $\sigma(x)$ is related to $\phi(x, y)$ by the Gauss' law:

$$\sigma(x) = -\frac{1}{2\pi} \frac{\partial\phi}{\partial y} \Big|_{y=0^+}. \quad (\text{S18})$$

In the incompressible region the contribution to charge density due to the first two terms of Eq. (S17) vanishes. This fixes the relation u_3 in terms of the LL density as:

$$u_3 = 2\pi\tilde{e}n_{\text{LL}}. \quad (\text{S19})$$

Next, the condition that the tangential electric field must vanish at the boundary of the incompressible region yields a relation between coefficients u_1 and u_2 :

$$u_1 = -\pi u_2 a^2. \quad (\text{S20})$$

Combining Eq. S20 with Eq. S18 gives the charge density:

$$\sigma(x) = \tilde{e}n_{\text{LL}} + \frac{u_2}{\pi} \begin{cases} \sqrt{x^2 - a^2} & \text{for } x > a \\ 0 & \text{for } -a < x < a \\ -\sqrt{x^2 - a^2} & \text{for } -a < x \end{cases}. \quad (\text{S21})$$

Finally, since the dependence at $x \gg a$ is linear with x , we can express u_2 in terms of the charge density gradient $\frac{d\sigma}{dx}$ in the compressible region outside the incompressible strip:

$$\frac{d\sigma}{dx} \Big|_{x \gg a} = \frac{u_2}{\pi}. \quad (\text{S22})$$

This expression allows us to relate u_2 to the $\frac{dn}{dx}$ value, which was calculated numerically for a compressible droplet (see dashed line in Fig. 4B):

$$\tilde{e} \left. \frac{dn}{dx} \right|_{x=0} = \frac{u_2}{\pi}. \quad (\text{S23})$$

Using the fact that the drop of the electrostatic potential across the dipolar incompressible strip is $\Delta\epsilon_{LL}/\tilde{e}$, we get:

$$\tilde{e}u_1 = -\Delta\epsilon_{LL}, \quad (\text{S24})$$

where $\Delta\epsilon_{LL} = \hbar v_F \sqrt{2}/l_B$ is the average LL energy spacing.

Combining Eqs. S21, S23 and S24, we obtain the width of the incompressible region

$$l = \left(\frac{4\Delta\epsilon_{LL}}{\pi^2 \tilde{e}^2 \left. \frac{dn}{dx} \right|_{x=0}} \right)^{\frac{1}{2}} \approx 34 \text{ nm}, \quad (\text{S25})$$

as quoted in Eq. 4 in the main text and $\tilde{e}^2 = \frac{e^2}{4\pi\epsilon_0\kappa_{ave}}$. Here we used the average dielectric

constant of the substrate and vacuum $\kappa_{ave} = (\kappa_{SiO} + 1)/2$, the Landau level spacing

$\Delta\epsilon_{LL} = \hbar v_F \sqrt{2}/l_B$ for the observed levels $N=0$ and -1 , and the density gradient $\frac{dn}{dr} \approx$

$3.9 \times 10^{22} \text{ m}^{-3}$ for the compressible droplet in the middle of the would-be incompressible

region (dashed line in Fig. 4B). We note that Eq. 20 in Ref. (5) has a similar form, except

for a numerical prefactor 2 instead of the prefactor 4. The two expressions are in

agreement in the limit of the substrate's dielectric constant being much greater than that

of vacuum as assumed in Ref. (5). In the case that the substrate's dielectric constant is

comparable to that of the vacuum, then Eq. S25 is more accurate.

The estimate in Eq. S25 is slightly greater than the width inferred from our measurement results shown in Fig.4E of the main text. The small discrepancy can be attributed to the result of Ref. (5), derived for LL spacing $\Delta\varepsilon_{LL}$ much smaller than the external potential, being used in the regime when $\Delta\varepsilon_{LL}$ is not small on the $V_B(r)$ scale. In this case, in contrast to Ref. (5), the incompressible strip width l is not small compared to the QHE droplet radius. These estimates may also be affected by renormalization of κ_{ave} due to interband polarization, which will be discussed elsewhere.

Movie S1. Experimental differential conductance, $g(V_b, V_g, \mathbf{r}, \mathbf{B})$, maps of the local density of states of the graphene QD in the x - y plane as a function of sample bias, V_b , indicated in the top center of the movie. The movie has four quadrants showing four different magnetic fields, 0, 1, 2, and 3 T. Various QD states are seen coming in at different bias, corresponding to the states observed in Fig. 2 of the main text. A smooth background was subtracted from each dI/dV spectra to remove the graphene dispersion in order to visualize all features on a single color scale.